Crumpling-origami transition for twisting cylindrical shells

Li-Min Wang,[1] Sun-Ting Tsai,[2] Chih-yu Lee,[3] Pai-Yi Hsiao,[4] Jia-Wei Deng,[1] Hung-Chieh Fan Chiang,[1] Yicheng Fei,[5] and Tzay-Ming Hong[1,*]

[1]*Department of Physics, National Tsing Hua University, Hsinchu 30013, Taiwan, Republic of China*

[2]*Department of Physics and Institute for Physical Science and Technology, University of Maryland, College Park, Maryland 20742, USA*

[3]*Hsinchu Senior High School, Hsinchu 30013, Taiwan, Republic of China*

[4]*Department of Engineering and System Science, National Tsing Hua University, Hsinchu 30013, Taiwan, Republic of China*

[5]*Department of Physics and Astronomy, Rice University, Houston, Texas 77005, USA*

(Received 14 October 2019; revised manuscript received 9 January 2020; accepted 17 April 2020; published 11 May 2020)

Origami and crumpling are two processes to reduce the size of a membrane. In the shrink-expand process, the crease pattern of the former is ordered and protected by its topological mechanism, while that of the latter is disordered and generated randomly. We observe a morphological transition between origami and crumpling states in a twisted cylindrical shell. By studying the regularity of the crease pattern, acoustic emission, and energetics from experiments and simulations, we develop a model to explain this transition from frustration of geometry that causes breaking of rotational symmetry. In contrast to solving von Kármán–Donnell equations numerically, our model allows derivations of analytic formulas that successfully describe the origami state. When generalized to truncated cones and polygonal cylinders, we explain why multiple and/or reversed crumpling-origami transitions can occur.

DOI: 10.1103/PhysRevE.101.053001

I. INTRODUCTION

Origami [1] produces regular creases on a membrane. By use of predefined ordered patterns or spontaneous buckling [2,3], it can be exploited to design deployable and robust deformable structures [4–6], self-folding machines [7], tunable metamaterials [8], DNA origami [9], curved structures [10], etc. From the geometrical perspective, these structures have the hallmarks of topologically protected behavior [11] and excellent capability of shrinking volume.

Unlike origami, crumpling generates random creases and configurations [12,13] that can not be predicted by classical mechanics. This property makes the crumpling structure nonreproducible. Note that it has nothing to do with plasticity. Even for a purely elastic membrane in simulation [12], the ridges and vertices will assume a different configuration each time we unfold and recrumple. However, it still follows several statistical rules, such as power-law behavior in acoustic emission [14,15] and force response [16,17], log-normal distribution for crease length [18], and logarithmic decay of the size and height of a crumpled ball with time under compression [17,19]. In the initial stage of crumpling, the kite model [20] can predict the ratio of stretching and bending energies on each ridge and how their sum increases with ridge length. As ridge-ridge interactions become important, how the resistance force, the average length, and the number of ridges vary with the radius of the crumpled ball have also been deduced by molecular dynamics simulation and experiments [13,21,22].

Although origami and crumpling exhibit distinct characteristics, we are interested in knowing whether they can appear in the same physical system. Related researches are the determination of symmetric and nonsymmetric folds in crumpling [12], wrinkle-to-crumple transition of elastic sheets on a liquid drop [23], wrinkle-to-fold transition of elastic interface under lateral compression [24], and creasing [25]. Because origami can be considered as a regular arrangement of creases, it seems likely that, if we can combine these researches, there may exist a crumpling-origami transition. Ostensibly this attempt is hard because these two transitions are defined by different order parameters. To describe the crease pattern, past theories have had to rely on numerical or asymptotic methods to solve von Kármán equations [26–30]. It is challenging to find exact solutions by these two approaches even for a flat membrane, much less solve cases with arbitrary shapes. A clue to incorporate the transition between origami and crumpling states is localization of stress [23,24]. In the following, we present a physical system that exhibits these two states and provides a phenomenological theory that not only enables exact solutions but also can be generalized to tackle different shapes of shell without invoking complicated differential geometry.

II. EXPERIMENT

The setup of the twisting machine is shown in Fig. 1. We roll up the paper sheet into a cylinder and join its seam by an invisible tape. Various lengths L and different materials are tested. Our proctocol is to twist until both ends of the cylinderical shell touch. When the shell is twisted, its length will be reduced and this will tilt the movable pedestal. This

*ming@phys.nthu.edu.tw

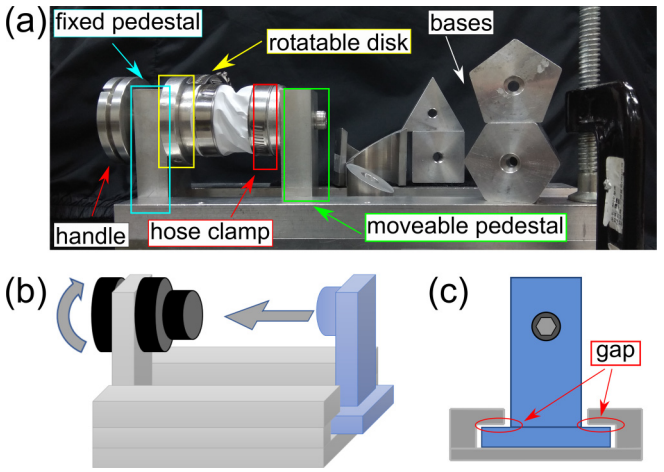

FIG. 1. (a) The base of the twisting machine can be switched from circular to polygonal. Hose clamps are employed to attach and seal the paper shell onto the base. Schematic plots of our machine are shown in panels (b) and (c). The base of movable pedestal was made of Bakelite to reduce friction. When a torque controlled by a stepper motor is applied to the handle, the cylinder will be shortened. This results in a self-tension that drives the movable pedestal toward the handle.

increases the normal force and the frictional force between the pedestal and the gap of track in Fig. 1(c). By lowering the height of the pedestal, we can decrease the moment arm of the force couple (shrink force, friction). Once the inclination of the pedestal is reduced, so is the friction that hinders its movement.

When L is shorter than the diameter $2R$, N pairs of regular valleys and ridges [2] appear almost simultaneously, indistinguishable by high-speed camera with 6000 fps, as shown in Fig. 2(a). In the mean time, a third kind of crease, which we term edges, develops on the boundaries of shell as they are deformed into regular N polygons. We denote this as the origami state. Figure 3(a) shows that $N = \sqrt{c(R/L) + d}$ only

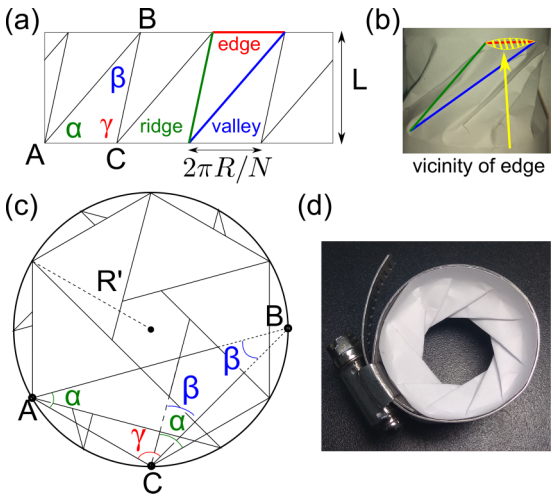

FIG. 2. Schematic plots in panels (a) and (c) show the geometry of creases after and before a twisted cylinder is unfolded. Panels (b) and (d) show the real sample.

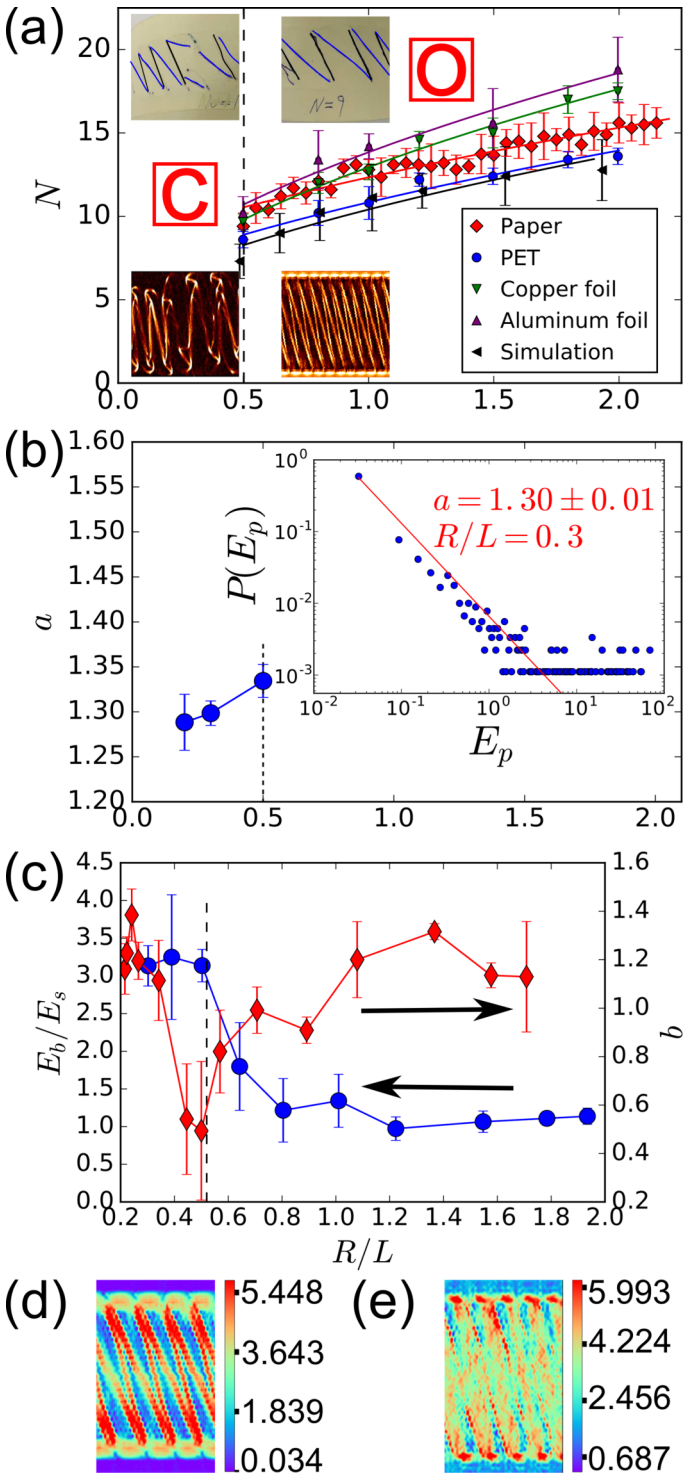

FIG. 3. Evidence for the transition of the CO state, marked by red squares, at $R/L = 0.5$ with an external tension of 302 gram weights. Panel (a) demonstrates that N can be well fit by the solid lines that follow $\sqrt{c(R/L) + d}$, where constants c and d are sample dependent [31]. Panel (b) shows how the exponent of $P(E_p) \sim 1/(E_p)^a$ varies with R/L. The inset demonstrates power-law behavior. Circles and diamonds in panel (c) depict the R/L dependence of E_b/E_s and b from molecular dynamics simulation. The topological mechanism that protects facets from bending is proved by the distribution of (d) bending and (e) stretching energies where the color bar denotes the relative energy value.

depends on the ratio [31] of R and L and is not sensitive to the twisting speed of 0.05–0.5 revolutions per second.

Unlike short cylinders, deformations for $L > 2R$ progressing from the boundaries are not symmetric and cause breakout of local buckling that is random in both time and space. The valleys and ridges that ensue not only differ in length but also may segment into multiple pieces, as in Fig. 3(a). We denote this as the crumpling state.

This crumpling-origami (CO) transition at $R/L \approx 0.5$ leaves its signature at acoustic emission. Our recording setup and detailed algorithms for counting the pulses have been described in Ref. [32]. Different from Ref. [14], the cylinder was twisted in only one direction. More than 40 pulses can be gathered for each trial in the crumpling state, compared to roughly 2 pulses for origami. The inset of Fig. 3(b) demonstrates that probability density function $P(E_p) \sim 1/(E_p)^a$, where E_p denotes the pulse energy—reminiscent of the crumpling process [14,15]. The exponent $a = 1.30$–1.34 in the range of $R/L = 0.3$–0.5 is determined by the maximum likelihood estimation, similar to a when crumpling the same material.

The simultaneous formation of ridges and valleys limits the number of sounds short cylinders can emit. Once the origami is formed, the topological mechanism [11] protects the faces between creases from further buckling and crackling noise. In contrast, the twisting of long cylinders shares the same local buckling as the crumpling processes, which occurs randomly in place and time. Therefore, it comes as no surprise that they share the same statistics for acoustic emission.

III. THEORETICAL MODEL

Why is the pattern of creases in origami triangular? We can argue it from three experimental facts in this state: (i) twisting symmetry, twisting one end by θ is indistinguishable from twisting both ends by $\pm\theta/2$; (ii) creases will follow the shortest path; and (iii) continuous rotational symmetry. Deformation on the cylinder surface is subject to rotation and will become slanted to the rotation axis. Fact (iii) requires the deformation be periodic. According to fact (ii) and elastic mechanics, the crease will be a straight line and appear at the place where deformation is the biggest [2]. Combining fact (ii) with fact (i), we are left with a triangular pattern.

Geometry dictates that the triangular pattern in Figs. 2(a) and 2(c) obeys $\alpha + \beta + \gamma = \pi$ and

$$\alpha - \beta + \gamma = \left(1 - \frac{2}{N}\right)\pi, \tag{1}$$

which gives $\beta = \pi/N$. We expect N comes from the competition of two potential energies. First is the energy stored in ridges and valleys, which clearly favors a small N. According to the simulation results in Fig. 3(c), this energy is proportional to the crease length. The aforementioned topological mechanism [11] rules out the interactions between ridges and valleys. We notice that, when the originally circular boundaries are deformed to polygons, the vicinity of each edge will be buckled as shown in Fig. 2(b). Presumably the longer the edge $2\pi R/N$ is, the more severe this buckling is. We expect the overlap of buckling from edges that face each other from opposite boundaries can be viewed as a repulsive potential. And since this interaction involves the buckling of two opposing edges, its strength is proportional to $(2\pi R/N)^2$ and inversely proportional to their distance. Overall, the energy consists of

$$E(N) = N\epsilon\left(\frac{L}{\sin\alpha} + \frac{L}{\sin\gamma}\right) + N\eta\left(\frac{2\pi R}{N}\right)^2\left(\frac{\sin\alpha}{L}\right), \tag{2}$$

where ϵ and η are phenomenological parameters.

Using the law of sines and the empirical fact that $N \gg 1$, we can approximate

$$\alpha \approx \sin^{-1}\sqrt{\frac{L}{2R}}. \tag{3}$$

By using Eqs. (1) and (3), we can minimize Eq. (2) and obtain

$$N \approx \pi\sqrt{\frac{\eta R}{\epsilon L}}, \tag{4}$$

which now depends only on η/ϵ. This expression describes well the trend in Fig. 3(a). Apparently the experimentally observed N has to be an integer. Since the predicted value in Eq. (4) is mostly not an integer, this implies an intrinsic randomness for N in our system.

Although experimentally N is not sensitive to external tension T and thickness t, their influence can be incorporated by adding a dimensionless correction [31], $T/(Yt^2)$, to Eq. (4), where Y is the Young's modulus.

The boundary of the CO transition is at $R/L \approx 0.5$. This is obvious from Eq. (3) because $\sin\alpha \leqslant 1$. An intuitive way to imagine this is that the projection of the longer crease in Fig. 2(c) on the base should never exceed twice the circumradius R' of the polygon in order for the structure to be fully foldable:

$$\frac{L}{\sin\alpha} \leqslant 2R\frac{\pi/N}{\sin(\pi/N)}. \tag{5}$$

Incorporating Eq. (4) in Eq. (5) gives a more rigorous expression for the threshold:

$$\frac{R}{L} \geqslant \frac{1}{2}\left(1 + \frac{2\epsilon}{3\eta}\right). \tag{6}$$

In origami, ridge-valley pairs are stable and arranged into predestined sites. In contrast, the excessive length of creases breaks the stable structure and renders their arrangement deviant from triangles. This frustration of geometry then leads to local buckling. The origami state can be viewed as an outcome of a reduction of continuous to discrete rotational symmetry. In the meantime, both rotational and twisting symmetries are broken by the emergence of local buckling in the crumpling state.

IV. SIMULATIONS

Besides Figs. 3(a) and 3(b), we search for more evidence of the CO transition from the energetics of creases and their interactions from molecular dynamics (MD) simulation. We construct the cylindrical shell by rolling up a thin sheet which was modeled by the triangular lattice with the bond length $r_0 = 1$. The elastic energy stored in the deformed shells contains two forms: the stretching energy $E_s = k_s(r - r_0)^2/2$ and the bending energy $E_b = k_b[1 - \cos(\theta - \theta_0)]$, where r denotes the distance between two adjacent beads, θ is the

angle spanned by three consecutive beads along a lattice direction, and θ_0 is the equilibrium angle.

The bending and stretching moduli are set to be comparable to realistic ones, where $(k_s, k_b) = (20\,000, 75)$. The effective thickness [22] t of the shell can be determined by $k_s/k_b = 3t^2/32$. If someone wants to simulate different elastic materials, it can be achieved by adjusting k_s but fixing k_s/k_b. The system is composed of 60 150 beads in total. The Lennard-Jones potential is used to ensure that no bead can penetrate each other. All simulations are performed using LAMMPS, version 16Mar18 [33].

During the simulation, we give every bead on both boundaries a constant angular velocity, making them rotate oppositely. We also let two boundaries move freely in the axial direction. The simulation result for number N versus R/L, plotted in Fig. 3(a), matches experiments. Its fitting parameters $(c, d) = (80.1, 28.3)$ imply $2\epsilon/3\eta = 2\pi^2/3c = 0.0821 \ll 1$, which agrees with our approximation $R/L \approx 0.5$ in Eq. (6) for the transition threshold.

Another proof of the CO transition is in the ratio of bending to stretching energies E_b/E_s for the whole cylinder, which changes from 1 to 3 in Fig. 3(c). Further evidence can be found in the same figure, which shows a dip in the transition for the exponent b in the scaling relation $E(\ell) \sim \ell^b$ for the total energy E stored in crease of length ℓ. After sampling the creases [31], we use the least-squares fitting to estimate b.

To argue the trend of b in Fig. 3(c), one needs to be reminded of the experience from the crumpling of flat sheets. In the initial stage of crumpling (stage 1), the creases are few and can be approximated as being independent. By use of the Kite model [20], $b = 1/3$ can be rigorously derived. A quick way to understand why the energy for doubling the length of a ridge is less than doubled is that the number of vertices remains at 2, not 4. As the crumpling proceeds and ridge-ridge interactions become important (stage 2), simulations [22] have shown that b increases to 1. Now letus go back to Fig. 3(c). (i) For the origami state, ridges and valleys extend across the boundaries of the cylinder and are devoid of vertexes. Therefore, $b = 1$ is expected. (ii) When R/L decreases and deviates from 0.5, the random creases increase in number and it is equivalent to moving from stage 1 to stage 2. As a result, b increases from roughly $1/3$ to 1.

As shown in Figs. 3(d) and 3(e), our simulations do not show any bending energy in the facets between creases, which supports the topological mechanism surmised by Ref. [11] from one dimension. An important question is whether ridges-valleys and edges are derived from the same mechansim of creasing. The answer is negative because E_b/E_s for ridges and valleys is larger than that for edges. The reason is explained in the following simulation process. The surface of the cylinder is originally buckled with both bending and stretching. Once the critical angle for creasing is reached, we observe that, while the stretching remains, bending on the buckled surface around ridges and valleys disappears due to the topological mechanism. In the meantime, the vicinity of edges continues to be both bent and stretched. The deformed edges on both boundaries of the cylinder are connected by the stretched facets that mediate their interaction, namely, the η term in Eq. (2).

V. GENERALIZATION

Next, we verify whether twisting or continuous symmetry triggers the CO transition. This can be tested by using more general Euclidean membranes, such as a truncated conical shell with R_1, R_2, and s, defined in the inset of Fig. 4(a). From experience, the degree of freedom can be reduced to $x \equiv R_1/s$ and $y \equiv R_2/s$. As expected, the buckling becomes irregular when s is too long. What is surprising is that this irregular state reoccurs at short s. In other words, there exist two CO transitions, as marked by the dashed lines in Fig. 4(d) for $(R_1, R_2) = (2.40, 4.95)$.

To clarify the source of this second transition, we have to resort to theoretical analysis. It turns out that Eqs. (1), (2), and (3) are still valid except for some modifications as delineated in the Supplemental Material [34]. The main mechanisms, crease formation and edge-edge interaction, also exist in the truncated cone. We can generalize the model in Sec. III and revise Eq. (2) to

$$E(N) = N\epsilon(\ell_v + \ell_r) + N\eta\left(\frac{2\pi R_1}{N}\right)\left(\frac{2\pi R_2}{N}\right)\frac{\sin\alpha_2}{s}, \quad (7)$$

where ℓ_v and ℓ_r denote the lengths of the valley and the ridge, and α_2 is defined in Fig. 4(b). One should notice that L in the second term of Eq. (4) becomes s in Eq. (7) because the edge-edge repulsion is now along the direction of s, as defined in the inset of Fig. 4(a). After some algebra [31], we obtain

$$N(x, y) \approx \pi\sqrt{\frac{x^2(x+y)(1+y-x)^2}{2y^2}\left(\frac{\eta}{\epsilon}\right)}, \; y \geqslant x, \quad (8)$$

and plot Fig. 4(f), which is consistent with the experimental data in Fig. 4(a).

An intuitive way to understand the second transition is to imagine the valley $\overline{AD}$ and the ridge $\overline{BD}$ that connect the two coaxial circles in Fig. 4(d). Apparently, geometry requires the origami state to obey

$$s \leqslant \overline{BD} \leqslant \overline{AD} \leqslant (R_1 + R_2)\frac{\pi/N}{\sin(\pi/N)}, \quad (9)$$

which reduces to Eq. (5) when $R_1 = R_2$. After some calculations, this inequality can be simplified to

$$(1 - x^2 + y^2)^2 \leqslant (x + y)(1 + y - x)^2, \quad (10)$$

which constrains the valid range of x and y for origami. Solid lines in Fig. 4(g) mark the state boundaries.

By now, we have shown that twisting symmetry is not crucial for CO transition by using truncated cones. How about rotational symmetry? In the following we lessen it from continuous to discrete by replacing the circular bases by m-polygons with circumradius R. The angle difference between the polygonal bases at either end of the shell is set to be zero. In order to seal and attach the shell tightly onto the bases, we insert circular segments into the space between hose clamp and bases. The lateral edges, as shown in Fig. 5(b), are predefined and made by bending and creasing the shell with the dihedral angle $\phi_p = \pi - 2\pi/m$. Note that we do not make these edges by folding, which is detrimental to the order-disorder transition in later discussions by affecting the deformation energy stored in the creases [35]. Unlike twisting

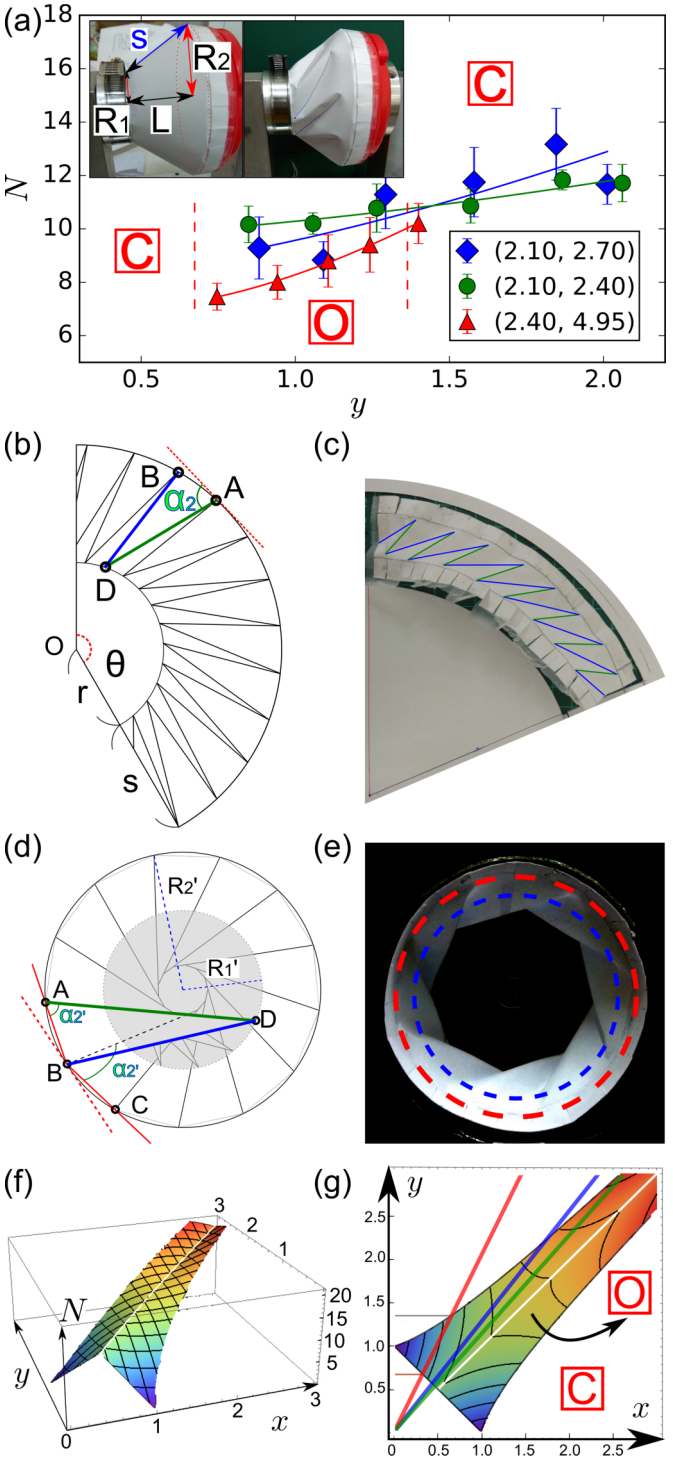

FIG. 4. The boundary of double CO transition for $(R_1, R_2) = (2.40, 4.95)$ is marked by the red dashed line in panel (a), which is the projection of the experimental data $N(x, y)$ onto the y axis. Solid lines from our theoretical predictions are consistent with the experimental results. Schematic plots and real samples are contrasted in panels (b) and (d) and panels (c) and (e), which exhibit the geometry of creases after and before a twisted cone is unfolded. The red/blue dashed line exhibits the circle with radius R_2/R_1. The three-dimensional surface in panel (f) describes the exact solution of $N(x, y)$. In panel (g), the red/blue/green line corresponds to $(R_1, R_2) = (2.40, 4.95)/(2.10, 2.70)/(2.10, 2.40)$, while the black line depicts the state boundary.

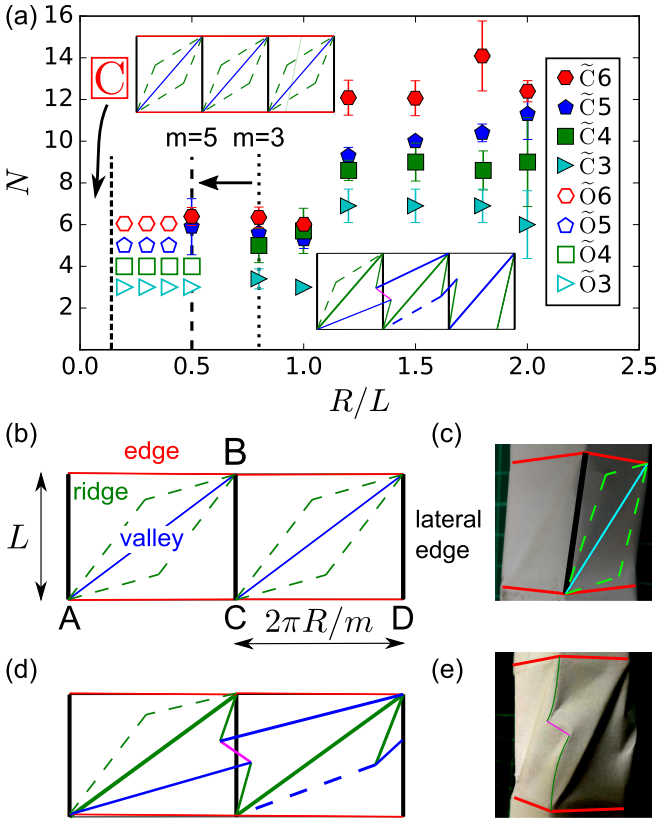

FIG. 5. Panel (a) shows the experimental data of m-polygons where $m = 3$–6. The legends $\widetilde{\mathrm{C}}$ and $\widetilde{\mathrm{O}}$ denote crumpling-like and origami-like states. The black arrow indicates how the boundary of the $\widetilde{\mathrm{OC}}$ transition decreases as m increases. The upper and lower insets show the schematic pattern of creases in the $\widetilde{\mathrm{O}}$ and $\widetilde{\mathrm{C}}$ states. Panels (b) and (d) are schematic magnified views of the upper inset in the $\widetilde{\mathrm{O}}$ and $\widetilde{\mathrm{C}}$ states with photos of the real sample in panels (c) and (e).

a circular cylinder shell, a polygonal shell is very sensitive to the coaxiality of the pair of bases. So it is hard to reproduce the following experimental results by twisting by hands.

Experimental results are shown in Fig. 5(a). When R/L is small, the creases are periodic with $N = m$, as plotted in the left inset, but the pattern becomes irregular as R/L gets too large, as in the right inset. We label these two states as $\widetilde{\mathrm{O}}$ and $\widetilde{\mathrm{C}}$ which can be distinguished by whether error bars δN equal zero or not. Note that not only are they distinct from the CO states in Figs. (3) and (4) but also their order during the transition is reversed.

Before giving a physical picture for the $\widetilde{\mathrm{O}}$ and $\widetilde{\mathrm{C}}$ states, we need to clarify the role of lateral edges, like $\overline{BD}$ in Fig. 5(b). They store bending energy with $\phi_p = \pi - 2\pi/m$ through localized plastic deformations [35]. The dislocation of the lateral edge will exclude [27] ridges and valleys from crossing it. This leads to $N = m$ in the $\widetilde{\mathrm{O}}$ state. However, N is observed to increase with R/L in the O state, which is consistent with the behavior of cylinders. We believe this dilemma between $\widetilde{\mathrm{O}}$ and O causes the nonperiodic pattern in the $\widetilde{\mathrm{C}}$ state that is dissimilar to the C state. Likewise, experience on cylinders also informs us that a C state must await at small R/L. As

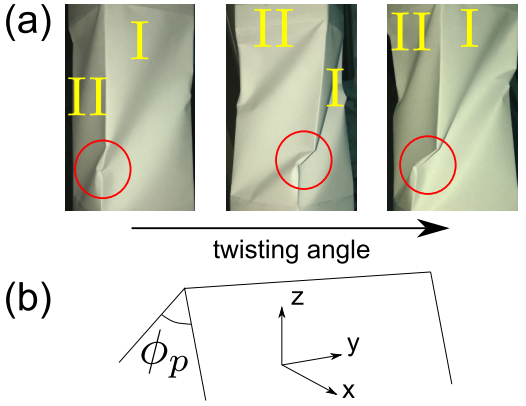

FIG. 6. The emergence and evolution of deformation on a square cylinder with folding lateral edges as the twisting angle increases from left to right in panel (a). Facet I has the feature of the $\widetilde{\mathrm{O}}$ state. In contrast, two valleys show up on facet II as a result of the lateral edge, marked by the red circle, being bent toward the x direction. The schematic plot of the lateral edge with ϕ_p in panel (b) facilitates the understanding of different resistances in the x and z directions.

a result, polygon cylinders can exhibit double CO transitions ($\mathrm{C\widetilde{O}\widetilde{C}}$).

Now we need to address the importance of m. A smaller m gives smaller ϕ_p and stronger exclusive interaction with ridges and valleys. Consequently, the range of $\widetilde{\mathrm{O}}$ will shrink when m increases, as shown in Fig. 5(a). It is thus expected that $\widetilde{\mathrm{O}}$ will disappear at some threshold m^* beyond which the influence of lateral edges becomes negligible and $\widetilde{\mathrm{C}}$ will be converted to the O state. In other words, the polygon with $m \geqslant m^*$ behaves no different from cylinders and exhibits only one crumpling-origami transition.

VI. CONCLUSIONS AND OUTLOOK

We presented an example of the existence of origami and crumpling states in the same physical system and demonstrated the diversities of their transitions in various Euclidean membranes. The distinctions between these two states are represented by the regularities of their creases, acoustic emissions, energy ratios E_b/E_s, and exponents of $E \sim \ell^b$. Our theory deduces that the instability and randomness in the crumpling state come from frustration of geometry. The connection between our phenomenological parameters and traditional material properties remains to be explored.

It will be fruitful to focus on the $\mathrm{C\widetilde{O}\widetilde{C}}$ transition and the switch between $\mathrm{C\widetilde{O}\widetilde{C}}$ and CO, such as finding m^*, the detail mechanism of pattern formation, and geometric conditions, and determining the phase diagram. In addition, the conjectured boundary of $\mathrm{C\widetilde{O}}$ needs to be verified in future experiments. Another interesting phenomenon in polygonal cylinder experiments that is worth further investigation is the following: What happens if we make lateral edges by folding instead of bending with ϕ_p, in other words, creating a more plastic deformation. As shown in Fig. 6(a), the valley can now overpass the lateral edge and disrupt the regular pattern. We believe this is due to the folding rendering a larger or smaller resistance for the lateral edge to the z- and x-directional force in Fig. 6(b). This results in some lateral edges being bent in the x direction while valleys overpass them and breaking the discrete rotational symmetry, which is an important precursor to the $\widetilde{\mathrm{O}}$ state.

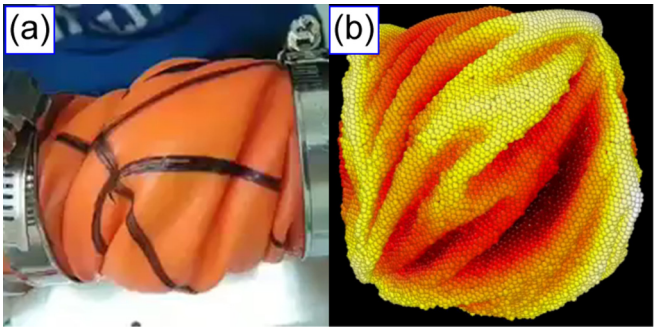

FIG. 7. Ridges and valleys can be seen to propagate roughly parallel to the rotational axis in (a) a twisted PVC ball with radius $\rho = 6$ cm and thickness $t = 1$ mm and (b) a simulated sphere [36] with $(k_b, k_s, \rho) = (2000, 10\,000, 40)$ and 23 087 beads.

Compared to truncated cones, it is reasonable to further investigate oblique circular cylinders. Generalization to non-Euclidean membranes, such as spheres, will be another challenge in both theoretical analyses and experimental realization. Preliminary results from our experiments and MD simulations in Figs. 7(a) and 7(b) show that ridges and valleys on a twisted sphere mostly follow a disorder pattern, but tend to be roughly parallel to the rotational axis. More work is needed to explore whether there is any regularity behind this phase.

ACKNOWLEDGMENTS

We gratefully acknowledge technical assistance from Mr. Zhen-Man Tian and financial support from MoST in Taiwan under Grants No. 105-2112-M007-008-MY3 and No. 108-2112-M007-011-MY3.

[1] Origami Resource Center, Origami Science. Retrieved from https://www.origami-resource-center.com/origami-science.html (2019).
[2] G. W. Hunt and I. Ario, Int. J. Non-Linear Mech. **40**, 833 (2005).
[3] C. Py, P. Reverdy, L. Doppler, J. Bico, B. Roman, and C. N. Baroud, Phys. Rev. Lett. **98**, 156103 (2007).
[4] Y. Nishiyama, Int. J. Pure Appl. Math. **79**, 269 (2012).
[5] Z. Song *et al.*, Nat. Commun. **5**, 3140 (2014).
[6] S. G. Li *et al.*, Proc. Natl Acad. Sci. USA **114**, 13132 (2017).
[7] S. Felton *et al.*, Science **345**, 644 (2014).
[8] J. L. Silverberg *et al.*, Science **345**, 647 (2014).
[9] P. W. K. Rothemund, Nature (London) **440**, 297 (2006).

[10] M. A. Dias, L. H. Dudte, L. Mahadevan, and C. D. Santangelo, Phys. Rev. Lett. **109**, 114301 (2012).
[11] B. Gin-ge Chen, B. Liu, A. A. Evans, J. Paulose, I. Cohen, V. Vitelli, and C. D. Santangelo, Phys. Rev. Lett. **116**, 135501 (2016).
[12] T. Tallinen, J. A. Astrom, and J. Timonen, Phys. Rev. Lett. **101**, 106101 (2008).
[13] Y. C. Lin, J. M. Sun, J. H. Hsiao, Y. Hwu, C. L. Wang, and T. M. Hong, Phys. Rev. Lett. **103**, 263902 (2009).
[14] P. A. Houle and J. P. Sethna, Phys. Rev. E **54**, 278 (1996).
[15] S. T. Tsai, C. D. Chang, C. H. Chang, M. X. Tsai, N. J. Hsu, and T. M. Hong, Phys. Rev. E **92**, 062925 (2015).
[16] G. A. Vliegenthart and G. Gompper, Nat. Mater. **5**, 216 (2006).
[17] Y. C. Lin, Y. L. Wang, Y. Liu, and T. M. Hong, Phys. Rev. Lett. **101**, 125504 (2008).
[18] D. L. Blair and A. Kudrolli, Phys. Rev. Lett. **94**, 166107 (2005).
[19] K. Matan, R. B. Williams, T. A. Witten, and S. R. Nagel, Phys. Rev. Lett. **88**, 076101 (2002).
[20] A. Lobkovsky *et al.*, Science **270**, 1482 (1995); A. J. Wood, Phys. A (Amsterdam, Neth.) **313**, 83 (2002); T. A. Witten, Rev. Mod. Phys. **79**, 643 (2007).
[21] Wubin Bai *et al.*, Phys. Rev. E **82**, 066112 (2010).
[22] S. F. Liou, C. C. Lo, M. H. Chou, P. Y. Hsiao, and T. M. Hong, Phys. Rev. E **89**, 022404 (2014).
[23] H. King, R. D. Schroll, B. Davidovitch, and N. Menon, Proc. Natl. Acad. Sci. USA **109**, 9716 (2012).
[24] L. Pocivavsek *et al.*, Science **320**, 912 (2008).
[25] M. Diab *et al.*, Proc. R. Soc., Ser. A **469**, 20120753 (2013).
[26] E. M. Kramer and A. E. Lobkovsky, Phys. Rev. E **53**, 1465 (1996).
[27] L. D. Landau and E. M. Lifshitz, *Theory of Elasticity*, 2nd ed. (Pergamon, Elmsford, NY, 1970).
[28] L. H. Donnell, NACA Report 479, 1933.
[29] N. Stoop *et al.*, Nat. Mater. **14**, 337 (2015).
[30] N. Yamaki, *Elastic Stability of Circular Cylindrical Shells* (Elsevier, Amsterdam, 1984).
[31] Effect of radius R, twisting speed ω, thickness t, external tension T, fitting parameters of different materials, and sampling process of creases are included in the Supplemental Material [34]. Less crucial details, such as precautions in experiments, can be found in L. M. Wang, master thesis (Physics, NTHU, Taiwan, 2018), retrievable from https://www.airitilibrary.com/Publication/alDetailedMesh?docid=U0016-1803201914484400.
[32] S. T. Tsai, L. M. Wang, P. Huang, Z. Yang, C. D. Chang, and T. M. Hong, Phys. Rev. Lett. **116**, 035501 (2016).
[33] S. J. Plimpton, J. Comput. Phys. **117**, 1 (1995).
[34] See Supplemental Material at http://link.aps.org/supplemental/10.1103/PhysRevE.101.053001 for detailed calculations.
[35] F. Lechenault, B. Thiria, and M. Adda-Bedia, Phys. Rev. Lett. **112**, 244301 (2014).
[36] H. C. Fan Chiang, L. J. Chiu, H. H. Li, P. Y. Hsiao, and T. M. Hong, arXiv:1910.02670.